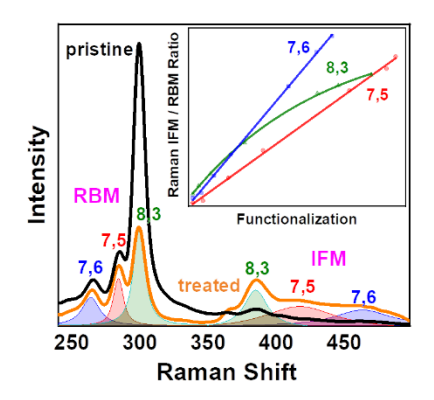
Structure-Resolved Monitoring of Single-Wall Carbon Nanotube Functionalization from Raman Intermediate Frequency Modes

Nima Soltani, † Yu Zheng, † Sergei M. Bachilo, † and R. Bruce Weisman*, †, ‡

ABSTRACT

Single-wall carbon nanotubes (SWCNTs) can be covalently modified to generate useful changes in their spectroscopic and photophysical properties. We report here a new method to monitor the extent of such functionalization reactions for different nanotube structures. Raman spectra are analyzed to find the intensities of structure-specific intermediate frequency mode (IFM) features in the range of ca. 350 to 650 cm⁻¹, which are induced by introduction of sp³ defects. The IFM frequencies are found to depend on both nanotube diameter and Raman excitation wavelength. The growth of IFM features is accompanied by a decrease in RBM intensities, so the IFM to RBM intensity ratio can provide a sensitive, structure-specific measure of nanotube functionalization.

TOC GRAPHIC



KEYWORDS Intermediate frequency mode, covalent functionalization, defect density, nanotube dispersive phonons, guanine functionalization reaction

[†] Department of Chemistry and the Smalley-Curl Institute, Rice University, Houston, Texas 77005, United States

[‡] Department of Materials Science and NanoEngineering, Rice University, Houston, Texas 77005, United States

Single-wall carbon nanotubes (SWCNTs) are a family of one-dimensional artificial nanomaterials that have attracted great attention because of their special physical and chemical properties and abundant potential applications. $^{1-3}$ A variety of discrete structural forms exist in samples of asproduced SWCNTs. Each structure is labeled by a pair of integers (n,m) and has particular optical and electronic properties that are determined by its diameter and chiral angle. $^{4-7}$ Recently, the intentional introduction of defects in SWCNT sidewalls through chemical reactions has greatly enhanced the versatility of structure-specific near-IR photoluminescence and advanced applications in bio-imaging and quantum information technologies. $^{8-14}$ The most common monitor of defects in SWCNT samples is the intensity ratio of D to G bands in Raman spectra. $^{15-18}$ This D/G intensity ratio reveals the extent to which sp^2 -hybridized carbon sites have converted to sp^3 defects. $^{19-22}$ However, although Raman radial breathing mode (RBM) frequencies are (n,m)-specific, 5,16,23 all (n,m) species contribute to the D and G band signals. Therefore, the D/G intensity ratios cannot reveal structure-resolved defect densities, and Raman characterization of defects in specific (n,m) species remains an unsolved problem.

Here, we report that (n,m)-specific intermediate frequency mode (IFM) Raman bands, with frequencies from 350 to 650 cm⁻¹, grow with introduction of defects to the SWCNT sidewall while the intensity of corresponding RBM bands decrease. The intensity ratio of IFM / RBM bands thus provides a new indicator of defect density in SWCNT samples. And because both IFM and RBM bands are (n,m)-specific, their ratio can be used to study covalent functionalization in particular nanotube structures.

To illustrate this approach, we use a recently discovered chemical reaction that is induced between SWCNT sidewalls and guanine nucleotides in the single-stranded DNA (ssDNA) coating the nanotube. This guanine functionalization reduces the nanotube band gap in a controllable,

patterned way and systematically red-shifts the SWCNT photoluminescence spectra.¹² The reaction proceeds spontaneously and rapidly at room temperature in the presence of singlet oxygen (¹O₂), which is formed through optical irradiation of rose bengal sensitizer, so the defect density in SWCNTs can be easily controlled by varying the ¹O₂ dose.¹² In this study, we prepared suspensions of HiPco SWCNTs coated by (GT)₂₀ and then exposed the samples to varying doses of ¹O₂ (see Figures S1 and S2). Figure 1a shows the 740 nm Raman spectra of the pristine and guanine-functionalized SWCNT samples. It can be seen that the intensities of RBM features decrease after the covalent functionalization, while there is a significant increase in IFM features from 350 to 550 cm⁻¹. We calculate the peak intensity ratio of IFM to RBM bands to monitor the introduction of covalent defects into the nanotube sidewalls. Raman spectra measured with different laser wavelengths showed the same growth of distinct IFM features and decrease of the RBM intensities (see Figure S3).

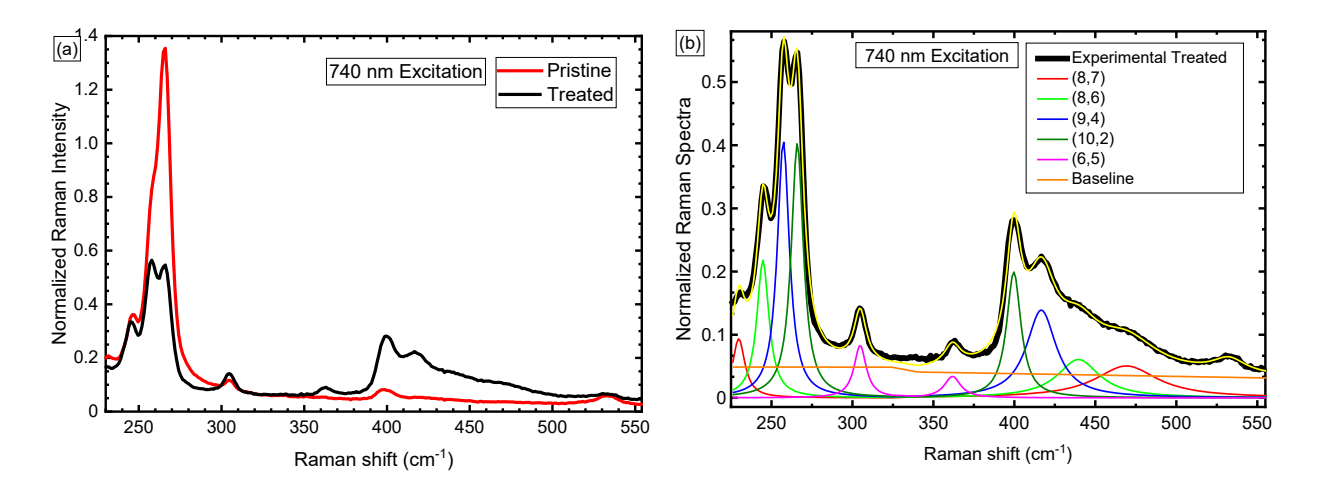


Figure 1. (a) Raman spectra, excited at 740 nm, of the pristine and guanine-functionalized SWCNT samples. (b) Raman spectrum of the guanine-functionalized sample (black trace) and (n,m)-specific components used to simulate it. The full simulated spectrum is plotted as a yellow curve that largely overlaps the black experimental trace.

It is well known that SWCNT Raman spectra are strongly resonance enhanced. The spectra are therefore dominated by features of those nanotube species that have electronic transitions close to

the Raman laser wavelength. ¹⁶ For this reason, the identities of SWCNTs giving Raman signals can be deduced by comparing the Raman excitation wavelength to allowed nanotube transitions, as well as by using the empirical relation between nanotube diameter and RBM frequency. ²⁴

We deduced the (n,m) assignment of the IFM bands by deconvoluting the spectra and carefully analyzing the spectral shapes to deduce the one-to-one correspondence between IFM peaks and known RBM (n,m) features. Both the RBM and IFM regions of each spectrum were fitted as sums of Lorentzian peaks to determine component peak positions, widths, and intensities. Then, analyzing several spectra, we observed intensity correlations between peaks in the two regions to help assign (n,m) values to the IFM features. This process was also aided by the inverse pattern of Raman shifts between IFM and RBM peaks (see eq 1 below). Figure 1b shows the deconvoluted 740 nm Raman spectra obtained by fitting the experimental spectra as a sum of Lorentzian basis functions. By similarly analyzing Raman spectra obtained using different laser wavelengths (see Figure S4), we found that the IFM frequencies of specific (n,m) species depend on the Raman laser wavelength as well as on nanotube diameter. Figure 2 shows IFM Raman shifts as a function of nanotube inverse diameter, measured at different excitation wavelengths. The strongly dispersive behavior (variation of Raman shift with excitation wavelength) suggests that the defect-assisted IFM band originates from a double resonance process involving a K-momentum phonon. The broad shape of the IFM features (Figure 1 and Figure S4) can be explained by the random nature of the scattering of photoexcited electrons by defects in a double resonance process.²¹

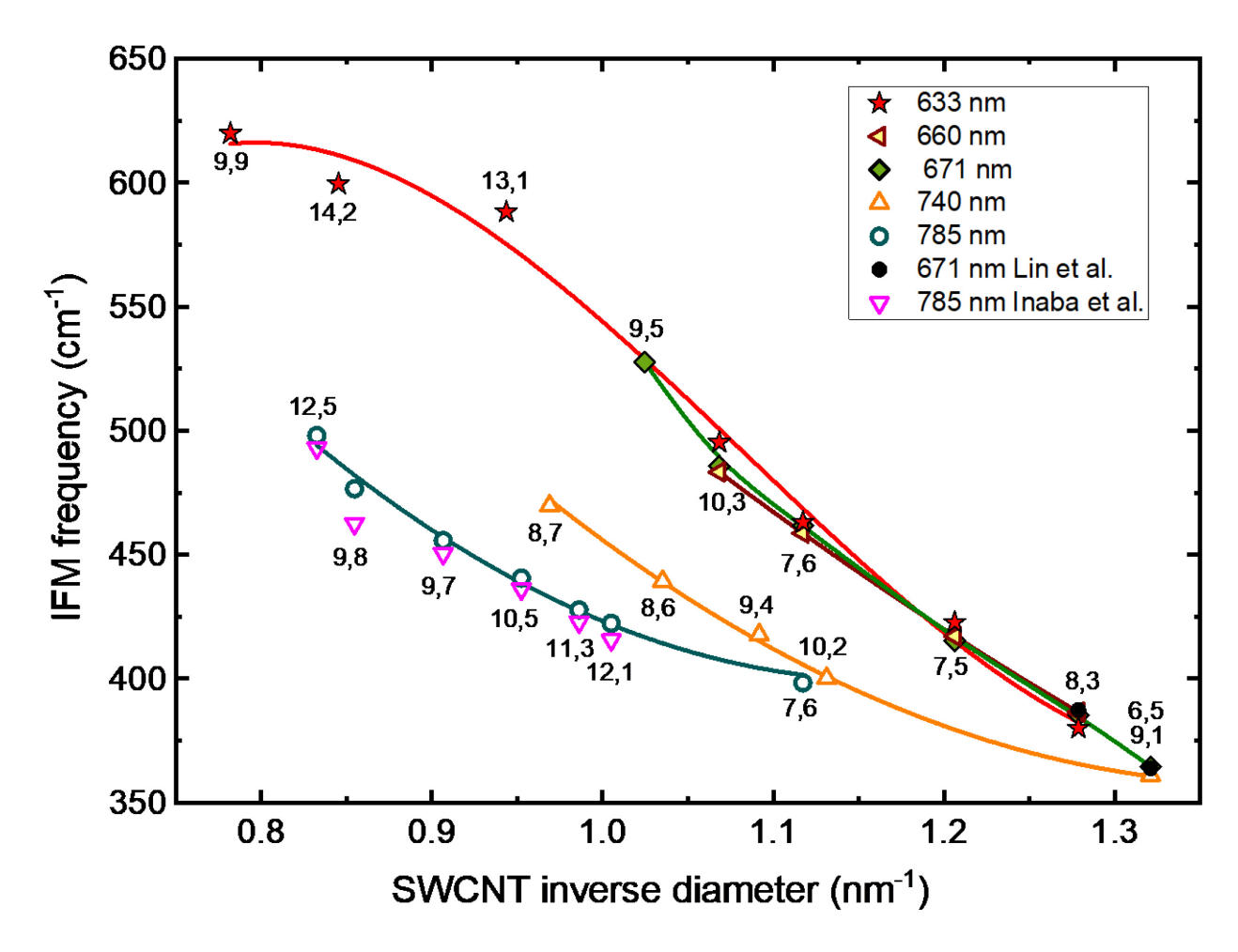


Figure 2. Measured IFM frequencies as a function of nanotube inverse diameter plotted for different excitation energies. Brown hexagons, violet squares, green diamonds, orange triangles, and red circles show IFM frequencies from Raman spectra obtained using 630, 660, 671, 740, and 781 nm excitation lasers, respectively. Two black filled circles show data published by Lin et al.²⁵ using a 671 nm laser. The magenta inverted triangles show experimental data points published by Inaba et al.^{26,27} Solid curves are guides to the eye.

Lin et al²⁵ have recently applied the same guanine-functionalization method to sorted samples of (9,1) and (8,3) SWCNTs. Figure 2 shows that the IFM frequencies of these sorted guanine-functionalized SWCNTs measured with 671 nm excitation are identical to the IFM frequencies we assigned by the above-mentioned fitting method. Moreover, we compared the IFM frequencies obtained by 785 nm excitation to the those observed by Inaba et al.^{26,27} using the same excitation wavelength. Inaba et al. used photobleaching to induce defects in individually suspended SWCNTs and then measured their Raman spectra. Figure 2 shows close agreement between their data and

our deduced frequencies, suggesting that the IFM band is a defect-induced feature of the nanotube itself and is not specific to the method or reaction used to introduce defects. The data in Figure 2 also show that for each individual excitation wavelength, the IFM frequency varies nearly linearly with inverse nanotube diameter, as long as the Raman excitation is in resonance with E_{22}^S . In other words, the plot of IFM frequency vs inverse nanotube diameter only diverges from linear behavior when the (n,m) species is excited through a side-band of E_{11}^S or through E_{11}^M for metallic nanotubes (see Figure S6c and its caption). These results strongly support the findings of Weight *et al.*²⁸ who used the coupled perturbed Hartree-Fock (CPHF) method with different laser wavelengths to simulate the defect-induced IFM Raman features. The results of their calculations showed that Raman spectra depend strongly on whether the incident photon couples to the E_{22} or E_{11} transition. They therefore suggested that multiple Raman laser wavelengths are needed to provide a complete view of nanotube phonons.^{28,29}

For E_{22}^S excited SWCNTs, we found that our data fit well to the following empirical relation between IFM frequency (ν_{IFM}), nanotube diameter (d_t), and incident photon frequency (ν_L):

$$\nu_{IFM} = \frac{336}{d_t} - 0.0558 \frac{\nu_L}{d_t} + 0.0906 \nu_L - 354 \tag{1}$$

Here, diameter is in nanometers and v_{IFM} and v_L are in cm⁻¹. Note that there is no apparent dependence on chiral angle. We also found that eq 2, with only two parameters, can be used as a simpler alternative empirical formula to describe the IFM frequency of a semiconducting SWCNT in terms of the nanotube diameter and excitation photon frequency, regardless of the resonance condition. (Table S2 compares alternative formulas with different numbers of parameters.)

$$\nu_{IFM} = 0.0281 \, d_t \, \nu_L + 66 \tag{2}$$

Values of the IFM dispersion factor and its dependence on SWCNT diameter were calculated from interpolated data in Figure 2. The results are shown in Figure S7. Figure S6a shows that for each excitation wavelength, the IFM frequency increases as the RBM frequency decreases. The increase in IFM frequency with diameter found here matches previous published reports. ^{26,27,30} However, our dependence of IFM frequency on excitation wavelength, as shown in Figure 2, is opposite to the results of Vierck *et al.*, who deduced that the IFM band derives from the out-of-plane acoustic phonon branch of graphene. ³⁰ Figure S6 illustrates the discrepant IFM results from the two studies. We suggest that further investigations are needed to clarify the nature and spectroscopic properties of these K-momentum phonons.

To explore the potential of IFM intensities for monitoring structure-specific functionalization, we performed a series of experiments in which different defect densities were introduced into SWCNT samples using the process described in Experimental Methods. Figure S8 shows that as the defect density increases, the intensities of D and IFM bands both increase, accompanied by a decrease in RBM intensity. The correlated increase of IFM intensity and D / G ratio with enhanced covalent functionalization confirms that the IFM band is indeed a defect-induced Raman feature.

Figure 3a to 3e show that the IFM / RBM intensity ratio is well correlated with the change in the SWCNT emission wavelength caused by guanine functionalization (as found from excitation-emission fluorescence mapping; see Figure S2). Therefore, the IFM / RBM ratio can be used as a novel parameter to monitor the extent of covalent functionalization of specific (n,m) species.

Figure 3f shows that ratio for (7,6) SWCNTs, measured with different Raman excitation wavelengths. As can be seen, the slope of the IFM / RBM ratio vs. fluorescence red shift depends on the Raman excitation wavelength. The strong dependence of both the IFM frequency and its

intensity on Raman excitation wavelength must therefore be taken into account when deducing defect densities from Raman spectra. Finnie et al. 29 and Laudenbach et al. 31 similarly suggested that the same consideration applies when inferring defect density from D/G intensity ratios, as their results showed that the D-band intensity depends on both defect density and Raman excitation wavelength. 29,31

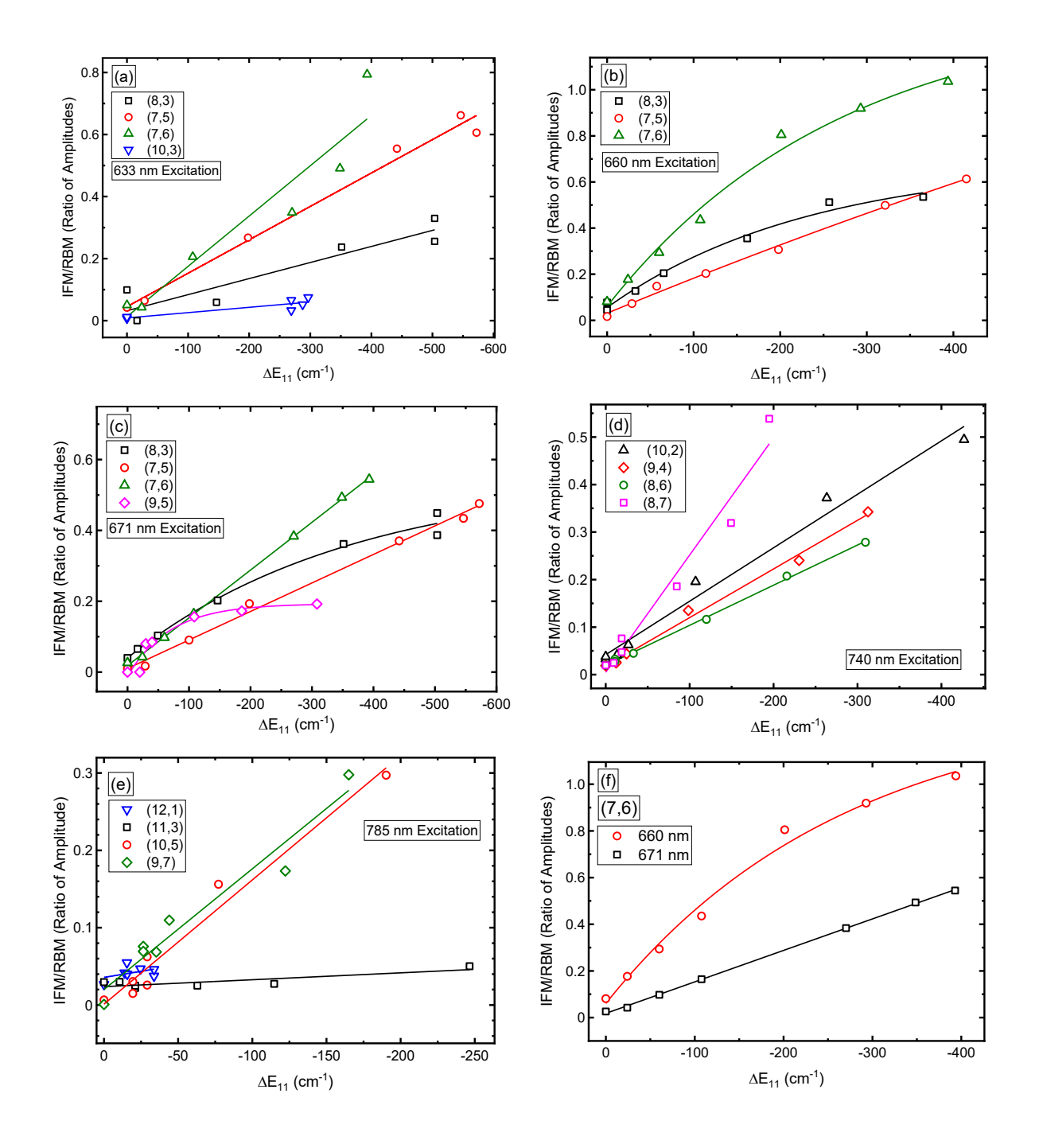


Figure 3. Ratio of IFM / RBM Raman amplitudes vs. fluorescence spectral shift from functionalization, for several labeled (n,m) species. Raman laser wavelengths were (a) 633 (b) 660 (c) 671 (d) 740 (e) 785 nm. (f) Ratio of IFM / RBM amplitudes for (7,6) SWCNTs measured with 660 and 671 nm excitation, plotted vs fluorescence spectral shift from functionalization.

We find that the D/G intensity ratio measured with 671 nm excitation is systematically larger than that measured with 740 nm (see Figure S9c), implying that the main nanotube structures

resonance-enhanced by 671 nm are more functionalized than those probed by 740 nm excitation. However, the more incisive IFM / RBM intensity ratios (see Figure S9d) reveal functionalization differences at the (n,m) level. To show that our method does not depend on nanotube source, we also tested it using SWCNTs grown by the CoMoCAT Method. The Raman spectra for pristine and treated CoMoCAT samples were measured with the 671 nm Raman laser (see Figure S11), which is near-resonant with the E₂₂ transition of (8,3). We found D / G and IFM / RBM intensity ratios of 0.36 and 0.50, respectively after treatment. Inaba et al²⁷ showed that for single chirality carbon nanotubes the IFM/RBM intensity ratio is equal to the D/G intensity ratio, i.e. $I_{IFM}/I_{RBM} = I_D/I_G$. However, we do not observe the same relationship for unsorted SWCNT samples, in which multiple species contribute to the D- and G-band intensities. For both of the SWCNT sources studied in the present work (HiPco and CoMoCAT), the IFM / RBM intensity ratio was larger than the D / G ratio. We suggest that carbonaceous impurities in SWCNT samples may contribute to D and G signals, thus lowering the sensitivity for probing SWCNT defects through the D/G intensity ratio, whereas RBM is a unique feature of SWCNTs, making the IFM / RBM ratio a more sensitive index of covalent defects.

Figure 4 shows that the IFM / RBM and IFM / G Raman intensity ratios can be used to monitor the extent of guanine functionalization in metallic carbon nanotubes, with the ratio increasing smoothly as the dose of singlet oxygen sensitizer increases. Since fluorescence spectroscopy cannot be used to monitor metallic SWCNTs, this provides the first reported evidence of guanine functionalization of metallic species.

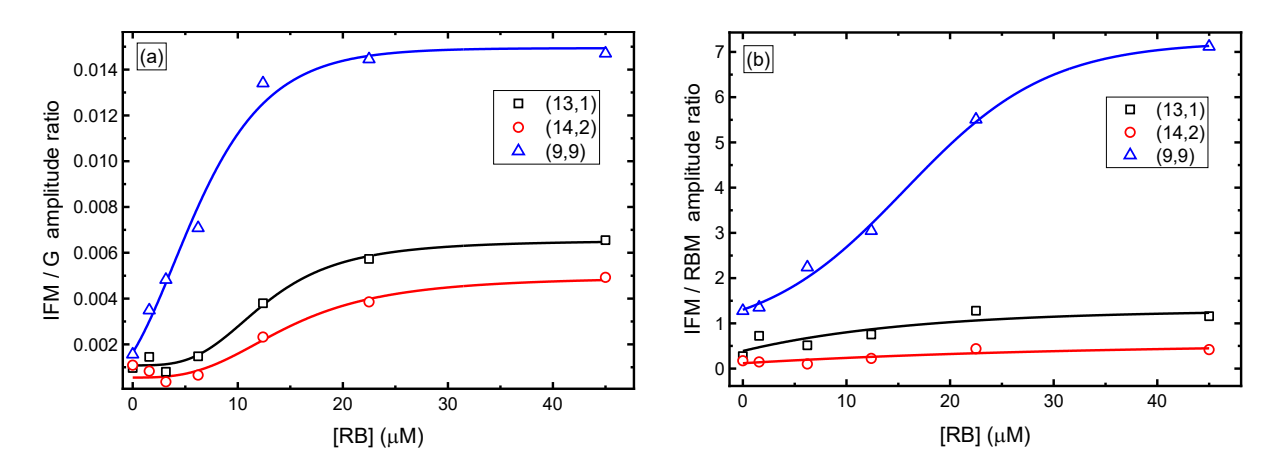


Figure 4. Increases in (a) IFM / G and (b) IFM / RBM Raman intensity ratios (with 633 nm excitation) in functionalized metallic SWCNTs. The x-axis shows the concentration of photosensitizer used to control the extent of covalent DNA functionalization.

The value of the IFM / RBM intensity ratio for characterizing (n,m)-specific covalent defects should also make it useful for finding differences in surfactant coating coverages among nanotube structures. We prepared dispersions of HiPco SWCNTs in 1% (w/v) sodium deoxycholate (SDC) and then exposed the sample to ozone. The fluorescence and 671 nm Raman spectra measured for the pristine and treated samples are shown in Figure 5. We observed that emission from (10,2), (7,6), and (9,4) SWCNTs was significantly quenched after O₃ exposure, whereas (6,5), (8,3), and (7,5) emission was relatively much less affected. This result agrees with findings of Hilmer et al. about selective emission quenching for SDC-dispersed SWCNTs after aryl diazonium treatment.³² We carefully analyzed fluorescence spectra to obtain the emission intensity ratio before and after O_3 exposure for individual (n,m) species. These quenching factors are summarized in Table 1 (see also Figure S12 and Table S3, which contains data extracted from both 671 nm and 740 nm Raman spectra). Table 1 also lists the IFM / RBM intensity ratios, which grow with O₃ exposure as the IFM band increases and the RBM band decreases. Raman spectra of the (7,6), (9,4), and (10,2) SWCNTs display large IFM / RBM intensity ratios, indicating that they acquire high densities of defects in the O₃ treatment, whereas the treated (8,3) and (7,5) nanotubes show negligible IFM features, implying little functionalization. The emission quenching factors are well correlated with

the Raman IFM / RBM ratios. We interpret the (n,m)-dependent spectral changes as reflecting differences in nanotube surface exposures when coated by SDC, with (8,3) and (7,5) SWCNTs better protected from dissolved O₃. Additional IFM / RBM intensity ratio findings are given in Supporting Information for ozone-treated suspensions in SDS and Pluronic-F12, and for diazonium-treated SDS suspensions.^{33,34} Our results demonstrate that Raman IFM / RBM ratios can be used to monitor general SWCNT covalent functionalization reactions.

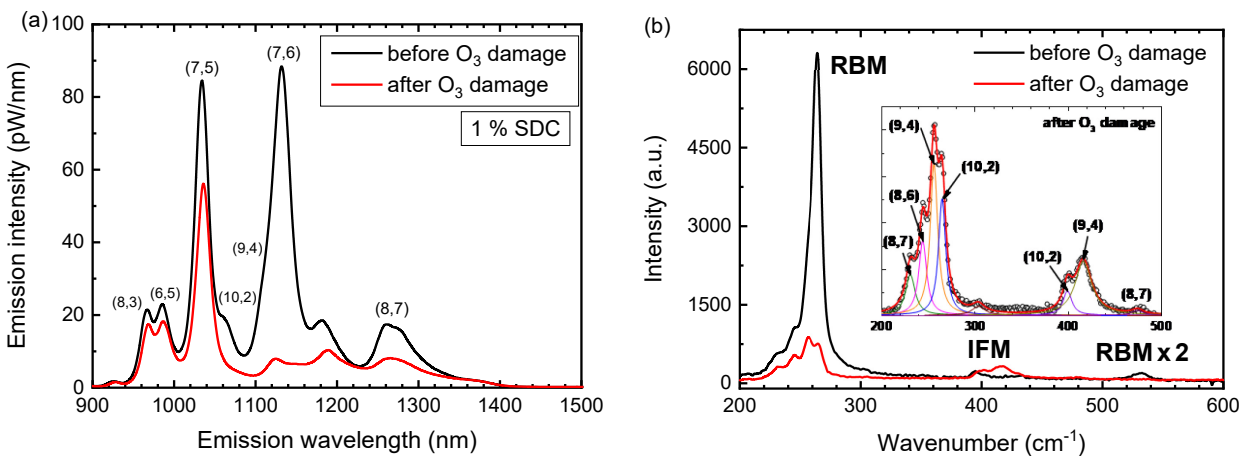


Figure 5 Fluorescence (a) and 671 nm Raman spectra (b) of SWCNTs suspended in a 1% SDC solution before (black curve) and after (red curve) O₃ exposure. The inset graph in (b) shows the deconvoluted Raman spectrum of SWCNTs exposed to O₃.

Table 1. IFM / RBM intensity ratios and fluorescence quenching factors from O_3 exposure, for six (n,m) species.

(n,m)	(8,3)	(7,5)	(7,6)	(10,2)	(9,4)	(8,7)
I _{IFM} / I _{RBM}	~ 0	~ 0	0.36	0.22	0.35	0.11
quenching factor	1.3	1.5	31	7	15	3

In summary, we have developed a methodology to characterize (n,m)-dependent defect densities in SWCNT samples. The frequencies of IFM Raman features between ca. 350 to 550 cm⁻¹ are found to depend on both nanotube structure and excitation wavelength in a pattern not previously reported. Increasing defect density causes a decrease in RBM intensity and a corresponding

increase in IFM intensity. The IFM / RBM intensity ratio can therefore serve as a quantitative monitor of (n,m)-specific covalent functionalization, with the aid of calibration data for the relevant SWCNT species and Raman excitation wavelengths. This method can also be used to assess (n,m)-specific exposures of nanotube surfaces to dissolved reactants.

Experimental Methods

SWCNTs that were grown in the Rice University HiPco reactor (Batch195.1) were added to an aqueous solution consisting of 60 mM phosphate buffer (pH=7.4), 100 mM NaCl, and 33 μM (GT)₂₀ ssDNA (purchased from Integrated DNA Technology, Inc.). The mixture was then cooled by an ice water bath and tip sonicated using a Branson model 250 Digital Sonifier at 35% output power for 45 active minutes (total time 90 min, with 30 s on and 30 s off duty cycle). The resulting suspension went through several cycles of 13000 x g centrifugation (Baxter Scientific Biofuge 13) and pellet removal. The final supernatant was used as the working (GT)₂₀-SWCNT suspension. In order to introduce sp^3 defects on the surface of SWCNTs in a controlled manner, we performed the guanine functionalization reaction¹² by adding rose bengal photosensitizer to the working suspension of nanotubes and irradiating with a green LED (emission spectrum shown in Figure S16), while keeping the sample at 15 °C in a water-jacketed cuvette. To modulate the level of functionalization, two different approaches were used: A) changing the irradiation time (30 s, 1 min, 2.5 min, 5 min, 10 min, or 20 min) using the same concentration of rose bengal (45.0 μM); or B) changing the concentration of rose bengal (0, 1.57, 3.13, 6.23, 12.4, 22.5, or 45.0 μM) and irradiating the samples for the same amount of time (2 h). Approach A) was used to functionalize the samples whose Raman spectra were measured by a 660 nm laser; approach B) was used to functionalize the samples that were measured with 633, 671, 740, and 785 nm lasers. Following the irradiation, residual rose bengal was washed from each sample using four successive dialysis

steps (24 h each) in a 100 kDa membrane dialysis tube against the phosphate buffer saline solution that was used to prepare the nanotube suspension ([phosphate]=60 mM, [NaCl]=100 mM, pH=7.4).

We used a custom-made apparatus to measure fluorescence excitation-emission maps in which the samples were excited by a tunable excitation source comprised of a SuperK Extreme supercontinuum laser and a Varia filter (NKT Photonics). A beam splitter directed a fraction of the excitation beam to a power meter to correct for intensity fluctuations of the excitation source. To block stray short-wave infrared (SWIR) emission, the excitation beam was passed through a KG5 short-pass filter (Schott). The sample was excited with a 5 nm bandwidth, scanning wavelengths from 520 to 830 nm with a step size of 5 nm. SWIR emission was collected at a 90° angle from excitation and passed through a long-pass dichroic mirror and then directly into the 300 μm core of an optical fiber placed close to the sample. The resulting emission spectra were measured by a BWTek Sol 1.7 spectrometer containing a 512-channel InGaAs array thermoelectrically cooled to −15 °C. The emission spectrum at each excitation wavelength was taken as the average of eight 150 ms acquisitions. Custom LabVIEW software controlled the instrument and acquired data.

We used prototype NanoSpectralyzer instruments (Applied NanoFluorescence, LLC) to measure Raman spectra with excitation wavelengths of 660 nm (3 s integration time, 10 averages), 671 nm (5 s integration time, 120 averages), and 740 nm (10 s integration time, 60 averages). A Renishaw inVia Raman microscope provided spectra with additional laser excitation wavelengths of 633 and 785 nm. For those measurements we used settings of 100% laser power, 10 s exposure time, and 20 accumulations.

ASSOCIATED CONTENT

Supporting Information: Absorption, emission, and Raman spectra showing the guanine

functionalization reaction; Deconvoluted Raman spectra of reaction products measured with

different laser wavelengths; Raman spectra and band intensity ratios as a function of reaction

extent and E₁₁ spectral shift; Raman spectra after reaction with ozone and diazonium salt.

AUTHOR INFORMATION

Corresponding Author

*E-mail: weisman@rice.edu. Tel: 713-348-3709

ORCID

Nima Soltani: 0000-0002-4264-6796

Yu Zheng: 0000-0003-2703-9143

Sergei M. Bachilo: 0000-0001-5236-1383

R. Bruce Weisman: 0000-0001-8546-9980

Notes

The authors declare the following competing financial interest: R.B.W. has a financial interest in

Applied NanoFluorescence, LLC, which manufactures the NanoSpectralyzer instruments used in

this project.

ACKNOWLEDGMENT

This research was supported by grant CHE- 2203309 from the National Science Foundation.

15

REFERENCES

- (1) Iijima, S.; Ichihashi, T. Single-Shell Carbon Nanotubes of 1-nm Diameter. *Nature* **1993**, *363* 603–605.
- (2) Dresselhaus, M. S.; Dresselhaus, G.; Saito, R. Physics of Carbon Nanotubes. *Carbon* **1995**, *33*, 883–891.
- (3) Dresselhaus, G.; Dresselhaus, M. S.; Saito, R. *Physical Properties of Carbon Nanotubes*; World Scientific, Singapore, 1998.
- (4) O'Connell, M. J.; Bachilo, S. M.; Huffman, C. B.; Moore, V. C.; Strano, M. S.; Haroz, E. H.; Rialon, K. L.; Boul, P. J.; Noon, W. H.; Kittrell, C.; Ma, J. P.; Hauge, R. H.; Weisman, R. B.; Smalley, R. E. Band Gap Fluorescence from Individual Single-Walled Carbon Nanotubes. *Science* 2002, 297, 593–596.
- (5) Bachilo, S. M.; Strano, M. S.; Kittrell, C.; Hauge, R. H.; Smalley, R. E.; Weisman, R. B. Structure-Assigned Optical Spectra of Single-Walled Carbon Nanotubes. *Science* **2002**, *298* 2361–2366.
- (6) Weisman, R. B.; Bachilo, S. M. Dependence of Optical Transition Energies on Structure for Single-Walled Carbon Nanotubes in Aqueous Suspension: An Empirical Kataura Plot. *Nano Lett.* 2003, 3, 1235–1238.
- (7) Zheng, Y.; Bachilo, S. M.; Weisman, R. B. Enantiomers of Single-Wall Carbon Nanotubes Show Distinct Coating Displacement Kinetics. *J. Phys. Chem. Lett.* **2018**, *9*, 3793–3797.
- (8) Ghosh, S.; Bachilo, S. M.; Simonette, R. A.; Beckingham, K. M.; Weisman, R. B. Oxygen Doping Modifies Near-Infrared Band Gaps in Fluorescent Single-Walled Carbon Nanotubes. *Science* **2010**, *330*, 1656–1659.
- (9) Lin, C.-W.; Bachilo, S. M.; Zheng, Y.; Tsedev, U.; Huang, S.; Weisman, R. B.; Belcher, A. M. Creating Fluorescent Quantum Defects in Carbon Nanotubes Using Hypochlorite and Light. *Nat. Commun.* 2019, 10, 2874.
- (10) Piao, Y.; Meany, B.; Powell, L. R.; Valley, N.; Kwon, H.; Schatz, G. C.; Wang, Y. Brightening of Carbon Nanotube Photoluminescence through the Incorporation of Sp 3 Defects. *Nat. Chem.* **2013**, *5*, 840–845.
- (11) Zheng, Y.; Bachilo, S. M.; Weisman, R. B. Photoexcited Aromatic Reactants Give Multicolor Carbon Nanotube Fluorescence from Quantum Defects. *ACS Nano* **2020**, *14*, 715–723.
- (12) Zheng, Y.; Bachilo, S. M.; Weisman, R. B. Controlled Patterning of Carbon Nanotube Energy Levels by Covalent DNA Functionalization. *ACS Nano* **2019**, *13*, 8222–8228.
- (13) He, X.; Hartmann, N. F.; Ma, X.; Kim, Y.; Ihly, R.; Blackburn, J. L.; Gao, W.; Kono, J.; Yomogida, Y.; Hirano, A.; Tanaka, T.; Kataura, H.; Htoon, H.; Doorn, S. K. Tunable Room-Temperature Single-Photon Emission at Telecom Wavelengths from sp³ Defects in Carbon Nanotubes. *Nat. Photonics* **2017**, *11*, 577–582.

- (14) Ma, X.; Hartmann, N. F.; Baldwin, J. K. S.; Doorn, S. K.; Htoon, H. Room-Temperature Single-Photon Generation from Solitary Dopants of Carbon Nanotubes. *Nat. Nanotechnol.* **2015**, *10*, 671–675.
- (15) Rao, A. M.; Richter, E.; Bandow, S.; Chase, B.; Eklund, P. C.; Williams, K. A.; Fang, S.; Subbaswamy, K. R.; Menon, M.; Thess, A.; Smalley, R. E.; Dresselhaus, G.; Dresselhaus, M. S. Diameter-Selective Raman Scattering from Vibrational Modes in Carbon Nanotubes. *Science* 1997, 275, 187–191.
- (16) Dresselhaus, M. S.; Dresselhaus, G.; Saito, R.; Jorio, A. Raman Spectroscopy of Carbon Nanotubes. *Phys. Rep.* **2005**, *409*, 47–99.
- (17) Dresselhaus, M. S.; Jorio, A.; Hofmann, M.; Dresselhaus, G.; Saito, R. Perspectives on Carbon Nanotubes and Graphene Raman Spectroscopy. *Nano Lett.* **2010**, *10*, 751–758.
- (18) Sebastian, F. L.; Zorn, N. F.; Settele, S.; Lindenthal, S.; Berger, F. J.; Bendel, C.; Li, H.; Flavel, B. S.; Zaumseil, J. Absolute Quantification of Sp3 Defects in Semiconducting Single-Wall Carbon Nanotubes by Raman Spectroscopy. *J. Phys. Chem. Lett.* **2022**, *13*, 3542–3548.
- (19) Graupner, R. Raman Spectroscopy of Covalently Functionalized Single-Wall Carbon Nanotubes. *J. Raman Spectrosc.* **2007**, *38*, 673–683.
- (20) Brown, S. D. M.; Jorio, A.; Dresselhaus, M. S.; Dresselhaus, G. Observations of the D-Band Feature in the Raman Spectra of Carbon Nanotubes. *Phys. Rev. B* **7**, *64*, 073403.
- (21) Saito, R.; Grüneis, A.; Ge, G. S.; Brar, V. W.; Dresselhaus, G.; Dresselhaus, M. S.; Jorio, A.; Cançado, L. G.; Fantini, C.; Pimenta, M. A.; Filho, A. G. S. Double Resonance Raman Spectroscopy of Single-Wall Carbon Nanotubes. *New J. Phys.* **2003**, *5*, 157.
- (22) Miyata, Y.; Mizuno, K.; Kataura, H. Purity and Defect Characterization of Single-Wall Carbon Nanotubes Using Raman Spectroscopy. *J. Nanomater.* **2011**, *2011*, 7.
- (23) Maultzsch, J.; Telg, H.; Reich, S.; Thomsen, C. Radial Breathing Mode of Single-Walled Carbon Nanotubes: Optical Transition Energies and Chiral-Index Assignment. *Phys. Rev. B* 11, 72, 205438.
- (24) Jorio, A.; Pimenta, M.; Souza Filho, A.; Saito, R.; Dresselhaus, G.; Dresselhaus, M. Characterizing Carbon Nanotube Samples with Resonance Raman Scattering. *New J. Phys.* **2003**, *5*, 139.
- (25) Lin, Z.; Beltrán, L. C.; De los Santos, Z. A.; Li, Y.; Adel, T.; Fagan, J. A.; Hight Walker, A. R.; Egelman, E. H.; Zheng, M. DNA-Guided Lattice Remodeling of Carbon Nanotubes. *Science* **2022**, *377*, 535–539.
- (26) Inaba, T.; Tanaka, Y.; Konabe, S.; Homma, Y. Effects of Chirality and Defect Density on the Intermediate Frequency Raman Modes of Individually Suspended Single-Walled Carbon Nanotubes. *J. Phys. Chem. C* **2018**, *122*, 9184–9190.

- (27) Inaba, T.; Homma, Y. Chirality Dependence of Electron-Phonon Matrix Elements in Semiconducting Single-Walled Carbon Nanotubes. *AIP Adv.* **2019**, *9*, 045124.
- (28) Weight, B. M.; Zheng, M.; Tretiak, S. Signatures of Chemical Dopants in Simulated Resonance Raman Spectroscopy of Carbon Nanotubes. *J. Phys. Chem. Lett.* **2023**, *14*, 1182–1191.
- (29) Finnie, P.; Ouyang, J.; Fagan, J. A. Broadband Full-Spectrum Raman Excitation Mapping Reveals Intricate Optoelectronic-Vibrational Resonance Structure of Chirality-Pure Single-Walled Carbon Nanotubes. *ACS Nano* **2023**, *17*, 7285–7295.
- (30) Vierck, A.; Gannott, F.; Schweiger, M.; Zaumseil, J.; Maultzsch, J. ZA-Derived Phonons in the Raman Spectra of Single-Walled Carbon Nanotubes. *Carbon* **2017**, *117*, 360–366.
- (31) Laudenbach, J.; Hennrich, F.; Telg, H.; Kappes, M.; Maultzsch, J. Resonance Behavior of the Defect-Induced Raman Mode of Single-Chirality Enriched Carbon Nanotubes. *Phys. Rev. B* **2013**, *87*, 165423.
- (32) Hilmer, A. J.; McNicholas, T. P.; Lin, S.; Zhang, J.; Wang, Q. H.; Mendenhall, J. D.; Song, C.; Heller, D. A.; Barone, P. W.; Blankschtein, D.; Strano, M. S. Role of Adsorbed Surfactant in the Reaction of Aryl Diazonium Salts with Single-Walled Carbon Nanotubes. *Langmuir* **2012**, *28*, 1309–1321.
- (33) Moore, V. C.; Strano, M. S.; Haroz, E. H.; Hauge, R. H.; Smalley, R. E.; Schmidt, J.; Talmon, Y. Individually Suspended Single-Walled Carbon Nanotubes in Various Surfactants. *Nano Lett.* **2003**, *3*, 1379–1382.
- (34) Kato, H.; Nakamura, A.; Horie, M. Behavior of Surfactants in Aqueous Dispersions of Single-Walled Carbon Nanotubes. *Rsc Adv.* **2014**, *4*, 2129–2136.